HHS Public Access

Author manuscript

Cell Rep. Author manuscript; available in PMC 2019 January 30.

Published in final edited form as:

Cell Rep. 2019 January 22; 26(4): 845–854.e6. doi:10.1016/j.celrep.2018.12.097.

Structural and Functional Studies of the RBPJ-SHARP Complex Reveal a Conserved Corepressor Binding Site

Zhenyu Yuan[1,4], **Bradley D. VanderWielen**[1,4], **Benedetto Daniele Giaimo**[2], **Leiling Pan**[3], **Courtney E. Collins**[1], **Aleksandra Turkiewicz**[2], **Kerstin Hein**[2], **Franz Oswald**[3], **Tilman Borggrefe**[2], and **Rhett A. Kovall**[1,5,*]

[1]Department of Molecular Genetics, Biochemistry and Microbiology, University of Cincinnati College of Medicine, Cincinnati, OH, USA

[2]Institute of Biochemistry, University of Giessen, Giessen, Germany

[3]Department of Internal Medicine I, Center for Internal Medicine, University Medical Center Ulm, 89081 Ulm, Germany

[4]These authors contributed equally

[5]Lead Contact

SUMMARY

Notch is a conserved signaling pathway that is essential for metazoan development and homeostasis; dysregulated signaling underlies the pathophysiology of numerous human diseases. Receptor-ligand interactions result in gene expression changes, which are regulated by the transcription factor RBPJ. RBPJ forms a complex with the intracellular domain of the Notch receptor and the coactivator Mastermind to activate transcription, but it can also function as a repressor by interacting with corepressor proteins. Here, we determine the structure of RBPJ bound to the corepressor SHARP and DNA, revealing its mode of binding to RBPJ. We tested structure-based mutants in biophysical and biochemical-cellular as-says to characterize the role of RBPJ as a repressor, clearly demonstrating that RBPJ mutants deficient for SHARP binding are incapable of repressing transcription of genes responsive to Notch signaling in cells. Altogether, our structure-function studies provide significant insights into the repressor function of RBPJ.

Graphical Abstract

*Correspondence: kovallra@ucmail.uc.edu.

AUTHOR CONTRIBUTIONS

R.A.K., T.B., and F.O. conceived and designed all of the studies. B.D.V., Z.Y., and C.E.C. performed the structural and ITC binding studies and the DSF experiments. B.D.G., A.T., and K.H. performed the assays in MT cells. F.O. and L.P. performed coimmunoprecipitation, the reporter assay, EMSA, and colocalization experiments. R.A.K. wrote the manuscript, and all authors reviewed and edited the manuscript.

SUPPLEMENTAL INFORMATION

Supplemental Information includes five figures and two tables and can be found with this article online at https://doi.org/10.1016/j.celrep.2018.12.097.

DECLARATION OF INTERESTS

The authors declare no competing interests.

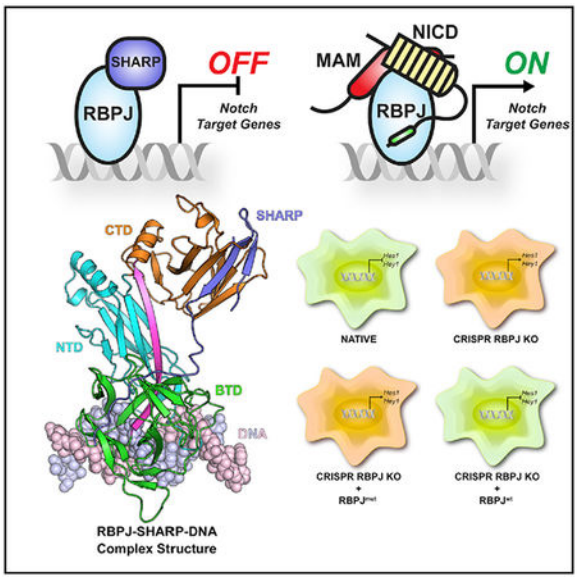

In Brief

Yuan et al. determine the X-ray structure of the corepressor SHARP bound to RBPJ, the nuclear effector of the Notch pathway. The structure-function analysis provides insights into corepressor binding to RBPJ and how RBPJ functions as a repressor of transcription of Notch target genes.

INTRODUCTION

The Notch pathway is a cell-to-cell signaling mechanism that is indispensable for cell fate decisions during prenatal development and postnatal tissue homeostasis (Kovall et al., 2017; Bray, 2016). Aberrant signaling underlies the pathogenesis of many human diseases, including certain types of cancer, congenital defects, and cardiovascular disease (Siebel and Lendahl, 2017). Given its association with human disease, there have been extensive efforts to identify reagents that pharmaceutically modulate the Notch pathway, with most efforts focused on modalities that curtail overactive Notch signaling (Braune and Lendahl, 2016). However, there is a need to identify targets that, when drugged, result in upregulated signaling to treat diseases associated with insufficient Notch activity (Siebel and Lendahl, 2017).

Signaling is initiated when Notch receptors interact with a DSL (Delta, Serrate, Lag-2) ligand, which results in proteolytic cleavage of Notch (Kovall and Blacklow, 2010). This releases the intracellular domain of Notch (NICD) from the cell membrane, allowing NICD to translocate to the nucleus. NICD directly binds the transcription factor RBPJ (recombining binding protein J-kappa, also known as CSL [CBF1/RBPJ, Su(H), Lag-1]) and recruits a member of the Mastermind (MAM) family of transcriptional coactivators (Mastermind-like [MAML1–MAML3] in mammals), resulting in transcriptional activation of Notch target genes (Borggrefe and Oswald, 2009). RBPJ can also function as a repressor by interacting with corepressor proteins such as SHARP (SMRT/HDAC1-associated repressor protein, also known as MINT [Msx2-interacting nuclear target] or SPEN [split

ends]) (Kuroda et al., 2003; Oswald et al., 2002), Hairless in *Drosophila melanogaster* (Maier, 2006), FHL1 (four and a half LIM domains 1, also known as KyoT2) (Taniguchi et al., 1998), L3MBTL3 (lethal 3 malignant brain tumor-like 3) (Xu et al., 2017), and RITA1 (RBPJ-interacting and tubulin-associated) (Tabaja et al., 2017; Wacker et al., 2011). Corepressors are part of higher-order transcriptional repression complexes that contain histone-modifying activity; e.g., histone deacetylase or histone demethylase, which convert chromatin into a transcriptionally repressed state (Borggrefe and Oswald, 2009).

Crystal structures have revealed that all RBPJ orthologs contain a conserved structural core composed of three domains, termed NTD (N-terminal domain), BTD (β-trefoil domain), and CTD (C-terminal domain) (Figures 1A and 1B; Wilson and Kovall, 2006; Nam et al., 2006; Kovall and Hendrickson, 2004). The NTD and CTD are immunoglobulin (Ig) domains that are structurally similar to the Rel homology region (RHR) of transcription factors such as NF-κB (nuclear factor κB) and NFAT (nuclear factor of activated T cells), whereas the fold of the BTD is related to cytokine and growth factor structures such as interleukin1 and FGF (fibroblast growth factor). The NTD and BTD form an electropositive surface that interacts with DNA. In the transcriptionally active RBPJ-NICD-MAM ternary complex bound to DNA (Figures 1A and 1B), the RBPJ associated molecule (RAM) and Ankyrin repeat (ANK) domains of NICD bind the BTD and CTD of RBPJ, respectively, whereas MAM interacts with the CTD-ANK interface and the NTD (Wilson and Kovall, 2006; Nam et al., 2006). In addition to the activator complex, several RBPJ-core-pressor structures have been determined, including the *Drosophila* corepressor Hairless bound to Su(H) (the fly RBPJ ortholog) (Yuan et al., 2016) as well as FHL1 and RITA1 bound to RBPJ (Tabaja et al., 2017; Collins et al., 2014). These studies reveal that Hairless binds the CTD of Su(H), whereas FHL1 and RITA1 bind the BTD of RBPJ, similar to the RAM domain of NICD.

SHARP is a large multidomain transcriptional coregulator protein that has folded functional domains separated by long intrinsically disordered regions (Figure 1B). Notably, SHARP has no sequence similarity with any of the previously identified corepressors that bind RBPJ. SHARP was originally identified in yeast two-hybrid screens for factors that interact with SMRT-NCoR and the transcription factor MSX2 (Shi et al., 2001; Newberry et al., 1999). SHARP has traditionally been thought of as a corepressor because it binds SMRT-NCoR through its C-terminal Spen paralog and ortholog C-terminal (SPOC) domain and represses transcription (Shi et al., 2001); however, it has also been shown that SHARP can recruit the KMT2D coactivator complex to Notch target genes (Oswald et al., 2016). Previously, we defined a region in SHARP that binds RBPJ, termed RBPID (RBPJ-interacting domain; Figure 1B) and showed that RBPJ and SHARP form a high-affinity complex (VanderWielen et al., 2011; Oswald et al., 2002).

Here we determine the X-ray structure of the RBPJ-SHARP corepressor complex bound to DNA. We identify structure-based mutants that are essential for RBPJ-mediated repression and characterize these mutants both *in vitro* and in cellular assays. Taken together, our studies reveal the conserved interface of the RBPJ-SHARP corepressor complex, which provides molecular insights into RBPJ repressor function, and identify a potential site on RBPJ that could be pharmacologically targeted to upregulate Notch signaling.

RESULTS

SHARP Forms a Bipartite Interaction with RBPJ

As shown in Figures 1C and 1D, SHARP interacts with two distinct surfaces on RBPJ, contacting its CTD and the BTD, which is consistent with previous binding studies (VanderWielen et al., 2011). Starting at the N terminus of its RBPID, SHARP forms a β-hairpin motif that binds between the two β sheets that compose the Ig domain of the CTD. The second β strand of SHARP, residues 2,788–2,794, pairs with β strand βg of the CTD, extending this from a three- to a five-stranded β sheet (Figure 1E). The SHARP-CTD interaction is followed by a short linker region that is poorly ordered and makes no contacts with RBPJ. The C-terminal portion of the SHARP RBPID binds in an extended fashion across the BTD in a manner that is structurally similar to the RAM domain of NICD (Wilson and Kovall, 2006; Figures 1C and 1D). The complex between SHARP and RBPJ is mainly driven by hydrophobic interactions between nonpolar side chains on SHARP and the CTD and BTD of RBPJ (Figure 1D), with SHARP residues L2791 and I2811 largely anchoring its interaction with the CTD and BTD of RBPJ, respectively (Table 1; Figure S1). Additionally, there are key ionic interactions that appear to play auxiliary roles in complex formation, including salt bridges between E2786 of SHARP and R438 of the CTD (Figure 1E) and K2807 of SHARP and the BTD residue E259 (Figure 1D). It should also be mentioned that, when complexed with SHARP, RBPJ maintains similar contacts with DNA, suggesting that SHARP binding does not affect the affinity of RBPJ for DNA, which is consistent with previous binding studies (VanderWielen et al., 2011).

As shown in Figure 1E, SHARP binding to RBPJ induces a structural change in the CTD that results in translation of β strands βf and βg outward, modestly expanding the CTD by as much as ~4 Å. A significant structural rearrangement is also observed for the loop that connects strand βe with βf, which strikingly repositions W441 from a buried to a solvent-exposed conformation when comparing unbound RBPJ with the RBPJ-SHARP complex (Figure 1E). The repositioning of W441 allows E2786 of SHARP to form a salt bridge with R438 of RBPJ. This structural rearrangement has not been observed for any other RBPJ structure determined to date.

Structural Comparison of Coregulator Binding Sites on RBPJ

NICD, together with MAM and RBPJ, forms a transcriptionally active ternary complex (Kovall and Blacklow, 2010). NICD interacts with high affinity to RBPJ (Johnson et al., 2010; Friedmann et al., 2008; Del Bianco et al., 2008; Lubman et al., 2007), binding the BTD and CTD of RBPJ via its RAM and ANK domains, respectively (Wilson and Kovall, 2006; Nam et al., 2006). Figure 2A compares the interfaces SHARP and NICD-MAM use to interact with RBPJ, illustrating the overlap of these binding sites. There is partial overlap of the SHARP and ANK-MAM binding sites on the CTD of RBPJ, whereas there is completely overlapping binding of SHARP and the RAM domain of NICD on the BTD of RBPJ. Although SHARP and ANK-MAM use different strategies and target different key residues to interact with the CTD; clearly, binding of SHARP and binding of ANK-MAM to the CTD are mutually exclusive (Figure 2A). Despite the absence of sequence similarity between SHARP and the RAM domain of NICD, unexpectedly, SHARP interacts with the BTD in a

manner that is structurally virtually identical to how RAM as well as the corepressors FHL1 and RITA1 interact with the BTD (Figure 2B). As shown in Figure 2B, RAM and other coregulators that bind the BTD have a characteristic hydrophobic tetrapeptide sequence (-fWfP-) that is essential for binding the BTD and serves as the linchpin for high-affinity interactions. SHARP is lacking this and other conserved elements that contribute to interactions with the BTD (Johnson et al., 2010). However, structural alignment of SHARP with RAM and other BTD binders reveals some sequence conservation of hydrophobic residues that play important roles in SHARP-RBPJ complex formation, including I2804, A2806, I2808, I2811, and P2812 (Figure 2B).

The corepressor Hairless is the major antagonist of Notch signaling in *Drosophila* and directly binds the CTD of Su(H) (the fly RBPJ ortholog) with high affinity to repress Notch target gene transcription in flies (Yuan et al., 2016; Maier et al., 2011). Although there is no sequence similarity between SHARP and Hairless, these two corepressors have evolved to bind the same CTD interface on RBPJ and Su(H), respectively (Figures 2C and 2D). However, there are major structural differences in how SHARP and Hairless form complexes with the CTD. In contrast to SHARP, which only induces a modest conformational change in CTD, Hairless binding dramatically opens up the Ig domain of the CTD, interacting with residues that form the hydro-phobic core of the CTD (Yuan et al., 2016). This allows Hairless to bind exclusively to the CTD with high affinity (Maier et al., 2011).

The CTD is structurally similar to the Rel homology region–C-terminal (RHR-C) domains of transcription factors such as NF-κB and NFAT (Kovall and Hendrickson, 2004). Figure 2E shows an overlay of the CTD from RBPJ with the RHR-C domain from NFAT. Importantly, the CTD deviates from canonical RHR-C domains by the absence of β strand a′ (βa′), which lies between the two β sheets that compose the Ig domain of a canonical RHR-C domain. Strikingly, SHARP binding to the CTD serves as a structural surrogate for βa′, occupying this region in the complex structure (Figure 2E), which has interesting implications for how binding sites have developed on RBPJ and will be discussed further below (Figure 2F).

Binding Analysis of RBPJ and SHARP Mutants

To gain further insights into RBPJ-SHARP complex formation and SHARP function and to validate our structural studies, we used a combination of assays, both *in vitro* and in cells, to analyze structure-based mutants. As shown in Table 1 and Figure S1, we used isothermal titration calorimetry (ITC) to quantitate binding between SHARP and RBPJ mutants. SHARP binds RBPJ with high affinity (K_d ~ 5 nM), where binding is enthalpically driven and entropically unfavorable (Table 1), in accordance with the RBPID of SHARP being an intrinsically disordered region (VanderWielen et al., 2011). Consistent with its side chain burying ~84 $Å^2$ in the SHARP-CTD complex, mutation of L2791 to alanine (L2791A) in SHARP resulted in a more than 350-fold decrease in binding ($\Delta\Delta G°$ = 3.4 kcal/mol; Table 1; Figure 1D). The SHARP mutants V2789A and Y2793A also significantly reduced binding to RBPJ by more than 10-fold and more than 20-fold, respectively (Table 1; Figure S1), in agreement with these residues also burying considerable amounts of surface area at the SHARP-CTD interface (V2789 = 54 $Å^2$ and Y2793 = 118 $Å^2$) (Figure 1D). The side chain

of SHARP residue I2811 is buried at the BTD-SHARP interface (Figure 1D), lying within a small hydrophobic pocket and burying a substantial 160 Å2. Mutation of I2811 to alanine (I2811A) results in more than a 60-fold reduction in binding (Table 1; Figure S1). Mutation of K2807 (K2807A), which makes electrostatic interactions with E259 of the BTD (Figure 1D), results in a much more modest effect on binding (~6 fold; Table 1; Figure S1). Consistent with SHARP binding independently to the BTD and CTD, which results in an avidity effect (VanderWielen et al., 2011), single alanine mutants are unable to completely abrogate binding. However, the SHARP double mutant L2791A/I2811A, which targets mutations to key residues that interact with the BTD and CTD (Figure 1D), results in a complete loss of binding in our ITC studies (Table 1).

Similarly, we performed ITC binding studies with structure-based RBPJ mutants and native SHARP. As controls, we performed differential scanning fluorimetry (DSF) to confirm that our RBPJ mutants were correctly folded (Figure S2A), electro-phoretic mobility shift assay (EMSA) to show that our RBPJ mutants bind DNA similarly to wild-type (WT) (Figure S2B), immunofluorescence microscopy to demonstrate that our RBPJ mutants properly localize to the nucleus (Figure S2C), and coimmunoprecipitation (coIP) from cells to show that our RBPJ mutants still bind NICD (Figure S2D). However, we were unable to purify and test, by ITC, some RBPJ mutants that target key residues in the CTD-SHARP complex (e.g., F468A) because these residues are buried within the hydrophobic core of the CTD and are required for proper folding of RBPJ. Nonetheless, as shown in Figures 1D and S1 and Table 1, mutation of L388 (L388A), which buries ~103$Å^2$ in the complex, results in an approximately 70-fold reduction in binding, whereas the CTD mutants L386A, L397A, and L466A had only a minor effect on SHARP binding (Table 1; Figures 1D and S1), consistent with these residues burying much less surface area at the CTD-SHARP interface (L386 = 39 $Å^2$, L397 = 3 $Å^2$, and L466 = 44 $Å^2$). Because SHARP binds the BTD of RBPJ in a structurally similar manner as the RAM domain of NICD and the corepressors FHL1 and RITA1, we used a set of alanine mutants (F261A, V263A, A284V, and Q333A) that we previously characterized for RAM, FHL1, L3MBTL3, and RITA1 binding to RBPJ (Figures 1D and S1; Table 1; Xu et al., 2017; Tabaja et al., 2017; Collins et al., 2014; Yuan et al., 2012). The BTD mutants F261A and A284V, which are more centrally located in the SHARP-BTD interface, have a stronger effect, significantly reducing binding by ~45-fold and ~50-fold, respectively (Figures 1D and S1; Table 1). V263A and Q333A, which significantly reduced RAM binding to RBPJ (Yuan et al., 2012) but target more peripheral interactions in the BTD-SHARP complex, only modestly affect binding (Figures 1D and S1; Table 1). Interestingly, similar binding trends were observed when these BTD mutants were previously tested for interactions with FHL1 and RITA1 (Tabaja et al., 2017; Collins et al., 2014). We also tested our SHARP mutants and a subset of our RBPJ mutants in cells using coIP of exogenously expressed RBPJ and SHARP RBPID proteins and a mammalian two-hybrid assay (Figure S3). Overall, we observed excellent correspondence between our ITC binding studies and our cellular assays, supporting our structural studies.

RBPJ-SHARP Interaction Is Required to Repress Notch Target Genes

To investigate the contribution of RBPJ-SHARP interactions in the regulation of transcription in cells, we analyzed the Notch target genes *Hes1* and *Hey1* in a mature T cell

line (MT) that lacks Notch activity (Xu et al., 2017). To interfere with RBPJ-SHARP-mediated repression in MT cells, we expressed the RBPID of SHARP as a GFP fusion protein either as the WT (GFP-SHARP/RBPID^{WT}) or the RBPJ-interacting defective mutant L2791A/I2811A (GFP-SHARP/RBPID$^{LI/AA}$) (Figure 3A). Expression of GFP-SHARP/RBPID^{WT} leads to the upregulation of *Hes1* and *Hey1*; i.e., derepression (Figure 3A). Moreover, this upregulation is associated with a concomitant increase in the active histone marks acetylation on histone H3 lysine 9 (H3K9ac) and H3K27ac without influencing nucleosome occupancy (Figures 3B–3D). Similar histone marks at *Hes1 and Hey1* are observed when Notch signaling is induced in MT cells (Figure S4). Expression of GFP-SHARP/RBPID$^{LI/AA}$ has little to no effect on *Hes1 and Hey1* expression or active histone marks (Figures 3A–3D). This suggests that GFP-SHARP/RBPID^{WT}, but not GFP-SHARP/RBPID$^{LI/AA}$, effectively outcompetes endogenous SHARP for binding to RBPJ, leading to derepression. Next we used CRISPR/Cas9 technology to deplete RBPJ (Figure 3E). Consistent with RBPJ repressor function, we observed robust upregulation of *Hes1* and *Hey1* in the absence of RBPJ (Figure 3E). Correspondingly, short hairpin RNA (shRNA)-mediated knockdown of RBPJ also resulted in upregulation of *Hes1* and *Hey1* (Figure 3F). Importantly, reintroduction of RBPJ^{WT} in the CRISPR/Cas9-mediated RBPJ-depleted background rescues the repression of *Hes1* and *Hey1* Notch target gene expression whereas the SHARP-interacting defective RBPJ mutant F261A/L388A (RBPJ$^{FL/AA}$) does not (Figure 3G). Altogether, our data demonstrate that the RBPJ-SHARP interaction is strongly required to repress transcription of Notch target genes in cells.

DISCUSSION

RBPJ forms an activation complex with NICD and MAM that is required to activate transcription from all Notch target genes. RBPJ can also function as a transcriptional repressor by interacting with corepressors; however, its role as a repressor, particularly in mammals, is not well understood. To address this gap, here we determine the X-ray structure of the RBPJ-SHARP corepressor complex bound to DNA and use a multitude of *in vitro* and cellular assays to characterize structure-based mutants to better understand RBPJ corepressor function.

Together with previous studies, the complex structure provides a detailed mechanism for how SHARP interacts with RBPJ to repress transcription. Prior to interacting with RBPJ, the RBPID of SHARP is intrinsically disordered (VanderWielen et al., 2011) and, upon binding, becomes structured, forming a bipartite interaction with RBPJ. As shown in Figures 1C–1E, the N-terminal portion of the RBPID assumes a β-hairpin motif that interacts with the CTD of RBPJ, resulting in a modest conformational change in the CTD; SHARP-CTD interactions are followed by a poorly structured linker and then an extended region that binds across a nonpolar surface on the BTD. Thus, SHARP forms a high-affinity complex with RBPJ by interacting with two distant binding surfaces, which, individually, have been shown previously to be of low affinity but, when tethered together, result in an avidity effect (VanderWielen et al., 2011). Importantly, it has also been shown previously that the affinity of RBPJ for SHARP is unaffected by whether it is bound to DNA (VanderWielen et al., 2011).

Our cellular studies clearly demonstrate that depletion of RBPJ in MT cells results in derepression of the well-established Notch target genes *Hes1* and *Hey1* (Figures 3E–3G). Moreover, rescue of repression by WT RBPJ, but not a SHARP-binding mutant, strongly suggests that SHARP is the primary core-pressor that mediates repression at Notch target genes in lymphocytes and, likely, other cells and tissues, which is consistent with previous *in vivo* studies of SHARP in mice (Surendran et al., 2010; Tsuji et al., 2007; Kuroda et al., 2003). These data are also consistent with research in other experimental systems showing that loss of RBPJ results in transcriptional derepression at some, but not all, Notch target genes (Chan et al., 2017; Castel et al., 2013). Why RBPJ-SHARP corepressor complexes are recruited to some Notch targets but not others remains an open question. Clearly, the RBPJ mutants described here, which affect SHARP interactions but leave NICD interactions largely intact, will be instrumental in addressing this and other questions regarding the repressor function of RBPJ.

In contrast to the RBPJ-NICD-MAM activator complex, RBPJ-corepressor interactions appear to be less conserved across disparate organisms. For example, although SHARP, also known as SPEN in *Drosophila* and DIN-1 in *C. elegans*, is conserved from nematodes to flies to mammals (Ariyoshi and Schwabe, 2003), the RBPID of SHARP is only conserved in vertebrates (VanderWielen et al., 2011). Similarly, the corepressor Hairless, which is the major antagonist of Notch signaling in *Drosophila*, is not conserved outside of insects and crustaceans (Zehender et al., 2017). However, although the corepressors that bind RBPJ are not strictly conserved across disparate organisms, interestingly, the corepressor binding sites on RBPJ are conserved. For example, SHARP, as well as the corepressors RITA1, FHL1, and, likely, L3MBTL3 binds to the BTD of RBPJ in a structurally similar manner (Figure 2B), and, strikingly, despite no sequence conservation between SHARP and Hairless, both proteins bind to the same cleft on the CTD of RBPJ (Figures 2C and 2D). Thus, it seems likely that other species-specific transcriptional corepressors that bind RBPJ will be identified, and they will likely utilize the aforementioned conserved binding surfaces on the BTD and CTD to interact with RBPJ.

In a broader context, RBPJ provides an interesting example for how ligand binding sites develop on proteins. As shown in Figure 2E, the canonical RHR-C fold, which is found in the transcription factors NF-κB and NFAT, contains a β strand, βa', that lies between β strands βa and βg; however, the CTD of RBPJ is missing βa' typically found in RHR-C domains. The ligand, in this case the corepressor SHARP, serves as a structural surrogate binding precisely in the region where the missing βa' strand would lie. Remarkably, this is the second instance in RBPJ where this has occurred. The first example, as shown in Figure 2F, was uncovered following the structure determination of the *C. elegans* RBPJ-NICD-MAM activation complex (Wilson and Kovall, 2006), where it was shown that the BTD of RBPJ is atypical because it deviates from the canonical β-trefoil fold so that it is missing two of the 12 strands of the consensus fold (Kovall and Hendrickson, 2004). In this case, the ligand, the RAM domain of NICD, again serves as a structural surrogate, binding across the BTD exactly where the two missing β strands would normally lie.

Finally, because of its association with human disease, there have been wide-ranging efforts to pharmacologically target the Notch pathway, but the majority of this work has focused on

re-agents that blunt overactive Notch signaling; e.g., in T cell acute lymphoblastic leukemia (Braune and Lendahl, 2016; Ntziachristos et al., 2014). However, there are numerous human diseases, including certain types of cancer, cardiovascular defects, and congenital syndromes, that are associated with insufficient Notch signaling (Siebel and Lendahl, 2017). Our structure-function studies provide a site on the CTD of RBPJ that could be druggable to block SHARP binding, leading to derepression of Notch target genes. This strategy has the potential to become a treatment option for diseases connected to deficiencies in Notch signaling.

STAR★METHODS

CONTACT FOR REAGENT AND RESOURCE SHARING

Further information and requests for resources and reagents should be directed to and will be fulfilled by the Lead Contact, Rhett A. Kovall (kovallra@ucmail.uc.edu).

EXPERIMENTAL MODEL AND SUBJECT DETAILS

E. coli strain Tuner(DE3) (Novagen) were grown at 37°C in LB media, induced with 0.1mM IPTG, and grown overnight at 20°C.

METHOD DETAILS

Overview of RBPJ-SHARP-DNA complex structure determination—In order to determine the X-ray structure of the RBPJ/SHARP corepressor complex bound to DNA, we purified recombinant RBPJ and SHARP proteins from bacteria, corresponding to the structural core of RBPJ (residues 53–474) and the RBPJ-interacting domain (RBPID) of SHARP (residues 2776–2820), formed complexes with a 13-mer oligomeric DNA duplex with single-stranded overhangs, containing a single RBPJ binding site, and screened the RBPJ/SHARP/DNA complex for crystallization conditions. While we were able to isolate crystallization conditions for the complex, despite extensive optimization efforts, we were unable to produce diffraction quality crystals amenable for structural analysis. Therefore, we produced an MBP (maltose binding protein) fusion protein with the RBPID of SHARP (MBP-SHARP), i.e., fixed-arm carrier approach (Moon et al., 2010), in which the MBP moiety also has surface entropy reduction mutations engineered into it, in order to identify crystallization conditions for the RBPJ/MBP-SHARP/DNA complex. This strategy successfully led to crystals that nominally diffract to 2.8Å resolution and belong to the space group $P2_1$ (a = 54.5Å, b = 231.6Å, c = 90.3Å, and β = 99.88°) (Table S1). We demonstrated that our MBP-SHARP construct binds RBPJ similarly as the native SHARP construct, albeit with somewhat weaker affinity (Figure S5B). This is likely due to the close crystal contacts between MBP and RBPJ required for crystallization of the complex. The RBPJ/MBP-SHARP/DNA complex structure was solved by molecular replacement and refined to a final R factor and free R factor of 19.4% and 22.8%, respectively (Table S1).

There are two RBPJ-MBP-SHARP/DNA complexes in the asymmetric unit (AU) of the crystals (Figure S5A) that overall are very structurally similar (RMSD 2.28 for 819 cα atoms), with even higher structural correspondence when either MBP (RMSD 0.07 for 297 cα atoms) or RBPJ (RMSD 0.66 for 388 cα atoms) are aligned individually (Figures S5C–

S5E). The largest structural difference between the two complexes in the AU is a poorly ordered linker region in SHARP (Figure S5F), whereby the different conformations are likely influenced by different environments within the crystals. For clarity in subsequent figures, we do not show the MBP moiety and all structural comparisons are performed with chains G & H of RBPJ and SHARP, respectively, as these proteins chains have overall lower temperature factors.

Protein expression and purification—The cloning, expression, and purification of *Mus musculus* core RBPJ, residues 53–474, and SMT3-SHARP, residues 2776–2833, which corresponds to the RBPJ-interacting region, were described previously (VanderWielen et al., 2011). Tuner *E. coli* (Novagen) were transformed with a GST-RBPJ (53–474) construct. Bacteria were grown at 37°C in LB medium, cooled to 20°C, induced with 0.1 mM IPTG, and grown overnight at 20°C. The bacteria were harvested by centrifugation and resuspended in PBS. The cell pellet was lysed by sonication, cleared by centrifugation and filtration, and subsequently loaded onto a glutathione-Sepharose column (GE Healthcare). The column was washed with PBS and the GST fusion proteins was eluted using reduced glutathione. The elutant was dialyzed and the GST tag cleaved with Precision Protease (GE Healthcare) per the manufacturer's protocol. A subsequent GST affinity column removed the GST moiety and RBPJ was further purified to homogeneity using ion exchange and size exclusion chromatography. An MBP-SHARP fusion protein was used to crystallize the RBPJ/SHARP/DNA complex. SHARP, corresponding to residues 2776–2820, was cloned into pMALX-E, which encodes maltose binding protein with the following surface entropy reduction mutations D82A, K83A, E172A, N173A, and K239A to aide in crystallization. The MBP-SHARP fusion construct was overexpressed in Tuner *E. coli* and cells were lysed by sonication. The lysate was incubated with amylose resin and eluted with 10 mM maltose. The MBP-SHARP fusion protein was further purified by size exclusion chromatography.

Crystallization and Data Collection—RBPJ/MBP-SHARP/DNA complexes were setup in a 1:1.1:1.1 molar ratio and screened for crystallization conditions using an Art Robbins Phoenix Crystallization Robot at 4°C. The RBPJ/MBP-SHARP/DNA complex crystallized in 100mM Bis-Tris pH 6.6, 100mM NaCl, 40% PEG 400, and 200mM NDSB-256. Crystals were harvested, flash frozen in liquid nitrogen, diffraction data were collected at the Advanced Photon Source, beamline 21-ID-F (LS-CAT). The RBPJ/MBP-SHARP/DNA crystals nominally diffract to 2.8Å and belong to the spacegroup $P2_1$ with unit cell dimensions a = 54.5Å, b = 231.6Å, c = 90.3Å, and β = 99.88°

Structure Determination, Model Building, and Refinement—Molecular replacement with Phaser (McCoy et al., 2007) was used to determine the RBPJ/MBP-SHARP/DNA complex structure using the following search models DNA (3BRG), RBPJ (3IAG), and MBP (3OB4). Two RBPJ/MBP-SHARP/DNA complexes were identified in the asymmetric unit. Phenix was used for the initial stages of refinement (Adams et al., 2010). Manual model building was performed with COOT (Emsley and Cowtan, 2004). TLS parameters were generated and the model was subsequently refined using BUSTER (Smart et al., 2012) and validated with MolProbity (Davis et al., 2007). The final RBPJ/MBP-SHARP/DNA model was refined to an R_{work} = 18% and R_{free} = 23% with good overall

geometry (see Table 1). PyMOL (The PyMOL Molecular Graphics System, Version 2.0 Schrödinger, LLC) was used to generate figures and perform structural overlays. The PISA server was used to analyze protein interfaces (Krissinel and Henrick, 2007).

Coordinates and structure factors have been deposited into the Protein Data Bank (6DKS)

Isothermal titration calorimetry (ITC)—ITC experiments were performed using a Microcal VP-ITC micocalorimeter. For all binding reactions, SMT3-SHARP (2776–2883) at ~100 μM was placed in the syringe and RBPJ (53–474) at ~10 μM was placed in the cell. Titrations consisted of an initial 1μl injection followed by 39 7μl injections. ITC binding experiments were performed in 50 mM sodium phosphate pH 6.5, 150 mM NaCl at 25°C. Samples were buffer matched using size-exclusion chromatography or dialysis. The raw data were analyzed using ORIGIN and fit to a one site binding model.

Cell culture and preparation of cell extracts—Mouse hybridoma mature T (MT) cell line was grown in Iscove's Modified Dulbecco Medium (IMDM, GIBCO) supplemented with 2% FCS, 0.3 mg/l peptone, 5 mg/l insulin, nonessential aminoacids and penicillin/streptomycin. Cells were grown at 37°C with 5% CO_2. HeLa (ATCC: CCL2), HEK293 (ATCC: CRL1573), 293T and *Phoenix*™ packaging cells (*Orbigen*, Inc., San Diego, CA, USA) were cultivated in Dulbecco's Modified Eagle Medium (DMEM, GIBCO) supplemented with 10% fetal calf serum (FCS) and penicillin/streptomycin. The MT Notch-ER system was previously described (Xu et al., 2017).

DNA transfection—HEK293 and HeLa cells were transfected using the Profectin and Lipofectamine 2000 transfection reagent, respectively, according to the manufacturer's instructions.

Coimmunoprecipitation experiments—HEK293 cells were transfected with the indicated constructs for expression of GFP- and Flag-tagged WT and mutant proteins. 24 hours after transfection cells were lysed with 600 μl CHAPS lysis buffer [10 mM 3-[(3-Cholamidopropyl)dimethylammonio]-1-propanesulfonate hydrate (CHAPS, Roth), 50 mM Tris-HCl (pH 7.8), 150 mM NaCl, 5 mM NaF, 1 mM Dithiothreitol (DTT, Merck), 0.5 mM Phenylmethanesulfonyl fluoride (PMSF, Merck) and 40 μl/ml "Complete Mix" protease inhibitor cocktail (Roche)]. The extracts were incubated with 40 μl agarose-conjugated anti-Flag antibody (M2, Sigma) at 4°C overnight. Precipitates were washed 6 to 8 times with CHAPS lysis buffer and finally resuspended in SDS-polyacrylamide gel loading buffer. For western blotting the proteins were resolved in SDS-polyacrylamide gels and transferred electrophoretically at room temperature to PVDF membranes (Merck) for 1 h at 50 mA using a Tris-glycine buffer system. The membranes were pre-blocked for 1 h in a solution of 3% milk powder in PBS-T (0.1% Tween 20 in PBS) before adding antibodies. The following antibodies were used: anti-GFP (7.1/13.1, mouse monoclonal IgG, secondary antibody peroxidase conjugated sheep anti-mouse IgG, NA931V, GE healthcare) or anti-Flag (M5, Sigma; secondary antibody, NA931V, GE healthcare).

***In vitro* protein translation—**The *in vitro* protein translations were performed using the TNT-assay (L4610) from Promega according to manufacturer's instructions. Prior to

EMSAs the *in vitro* translations of RBPJ (WT) and mutant proteins were monitored by western blotting using an anti-Flag antibody (M5, Merck).

Electro Mobility Shift Assay (EMSA)—Reticulocyte lysates from *in vitro* translations were used for electromobility shift assays (EMSAs) in a binding buffer consisting of 10 mM Tris-HCl (pH 7.5), 100 mM NaCl, 0.1 mM EDTA, 0.5 mM DTT, and 4% glycerol. For binding reaction, 2 μg poly(dI-dC) (GE healthcare) and approximately 0.5 ng of ^{32}P-labeled oligonucleotides were added. The sequence of the double-stranded oligonucleotide FO-233 (Key Resources Table) corresponds to the two RBPJ-binding sites within the EBV TP-1 promoter. Super shifting of complexes was achieved by adding 1 μg of anti-Flag (M5, Sigma) antibody. The reaction products were separated using 5% polyacrylamide gels with 1x Tris-glycine-EDTA at room temperature. Gels were dried and exposed to X-ray films (GE Healthcare).

Fluorescence microscopy—HeLa cells were cultured on glass coverslips at a density of 10^5 cells per cm^2. After 16 h cells were transfected with 400 ng of expression plasmids using the Lipofectamine 2000 transfection reagent (see above). 24 h after transfection cells were rinsed with PBS, fixed with 4% paraformaldehyde (PFA, Merck) in PBS (pH = 7.5). Specimens were embedded in “ProLong© Gold antifade” reagent (Thermofisher) supplemented with 2-(4-carbamimidoylphenyl)-1H-indol-6-carboximidamide (DAPI) and stored at 4°C overnight. Pictures were taken using a fluorescence microscope (IX71, Olympus) equipped with a digital camera (C4742, Hamamatsu), and a 100-W mercury lamp (HBO 103W/2, Osram). The following filter sets were used: Green, (EGFP) ex: HQ470/40, em: HQ525/50, blue (DAPI) D360/50, em: D460/50.

Luciferase assay—HeLa cells were seeded in 48-well plates at a density of 20×10^4 cells. Transfection was performed with Lipofectamine 2000 reagent (see above) using 1 μg of reporter plasmid alone or together with various amounts of expression plasmid (given in the corresponding figure legends). After 24 h luciferase activity was determined from at least four independent experiments with 20 μl of cleared lysate in an LB 9501 luminometer (Berthold) by using the luciferase assay system from Promega.

Infection of hybridoma mature T cell line—5×10^6 *Phoenix*™ cells were seeded and 24 h later they were transfected with the plasmid DNA of choice. Briefly, 20 μg of DNA were mixed with 860 μL of H_2O and 120 μL of 2 M $CaCl_2$ and mixed by vortexing. The DNA solution was transferred dropwise to 1 mL of 2 × HBS buffer (50 mM HEPES pH 7.05, 10 mM KCl, 12 mM Glucose, 280 mM NaCl, 1.5 mM $NaHPO_4$) while vortexing and the solution was incubated 20 min at room temperature. In the meantime, 25 μM Chloroquine solution (Sigma-Aldrich) was added to the *Phoenix*™ cells (1 μl/ml) and the cells were incubated for 10 min. The DNA solution was added to the cells and 12 h later the medium was replaced. After 24 h of incubation, the medium containing the retroviral suspension was filtered and Polybrene (Sigma-Aldrich) solution was added. Fresh medium was added to the *Phoenix*™ cells that were maintained in culture for further infections. The retroviral solution was used for spin infection of MT cells by centrifuging 45 min at 1800 rpm at 37°C. In total, four spin infections were performed over two days. Positively infected

cells were selected with puromycin (Serva) or blasticidin (GIBCO) and, eventually, GFP positivity was analyzed using a BD FACS Calibur

Generation of CRISPR/Cas9 depleted MT cells—CRISPR/Cas9 *Rbpj* depleted MT cells were generated as follows: 3×10^6 293T cells were seeded and, after 24 h, transfected with 2.5 μg psPAX, 1 μg pMD2G and 3.33 μg of the desired lentiCRISPR v2 vector using Lipofectamine 2000 Transfection Reagent (Invitrogen) accordingly to manifacturer's instructions. After at least 6 h of incubation at 37°C the medium was replaced with fresh one and 48 h post-transfection the supernatant was filtered, supplemented with polybrene and used for infection of MT cells. Positively infected cells were selected with puromycin and dilutions were performed to establish single cell clones. Individual clones were screened by western blotting versus RBPJ.

shRNA knockdown—For the knockdown in MT cells, the pLKO.1 TRC1 shRNA library (SIGMA-ALDRICH) was used. Transfection of 293T cells and infection and selection of MT cells was performed as previously described (Oswald et al., 2016). Sequence of the hairpins used in this study is indicated in Key Resources Table.

Constructs—The expression plasmid pcDNA3-Flag-mNotch-1-IC (Flag-NICD) and the luciferase reporter construct pGa981/6 (12 x CSL-RE-LUC) were previously described(Wacker et al., 2011). The Gal4-reporter plasmid pFR-Luc (5 x Gal4-RE-LUC) was previously described(Oswald et al., 2002). The pMSCV-FLAG-hRBPJ IRES Blasticidin was kindly provided by Dr. R. Liefke. All oligonucleotides used in this study are listed in Key Resources Table. PCR products were cloned in the pSC-A-amp/kan (Agilent Technologies 240205–5), digested with the selected restriction enzymes (New England Biolabs) and cloned into the destination vectors accordingly to Key Resources Table. All plasmids were analyzed by sequencing. The pcDNA 3.1 Flag2 (Invitrogen) was commercially acquired while the pMY BioTip60 IRES-GFP was previously described.

An engineered CRISPR/Cas9 resistant mouse RBPJ cDNA was synthetized at GENEART/Life Technologies and inserted into the pcDNA3.1 Flag2 via NotI digestion. The RBPJ mutants R218H, F261A, L388A and the F261A/L388A double mutant was generated by site directed mutagenesis using the QuikChange II XL Site-Directed Mutagenesis Kit (Agilent Technologies 200521–5) accordingly to manufacturer's instructions with primers listed in Key Resources Table and using the pcDNA3.1 Flag-mRBPJ wt CRISPR/Cas9 resistant plasmid as template. The mRBPJ wt and RBPJ F261A/L388A CRISPR/Cas9 resistant cDNAs were subcloned into the pMY-Bio-IRES Blasticidin. The mouse RBPJ-VP16 expression plasmids (pcDNA3.1-Flag-2-mRBPJ-VP16 wt, F261A, L388A and F261A/L388A) were constructed as follows: The stop codon was deleted by a mRBPJ specific PCR fragment (mRBP_VP16_UP, mRBPTAA_DO) resulting in the pcDNA3.1-Flag-2-mRBPJDstop constructs. A VP16 specific PCR-fragment (VP16_XhoI_UP, VP16_XbaI_DO) was inserted into the corresponding sites of pcDNA3.1Flag-2-mRBPJΔstop constructs resulting in the pcDNA3.1-Flag2-mRBPJ-VP16 plasmids. The Gal-4-Mint (2776–2833) and the EGFP-Mint (2776–2833) constructs were generated by PCR assisted cloning (Gal-Mint_F, Gal-Mint_R) into the BamHI/XbaI sites of pFa-CMV (Stratagene) and pEGFP-C1 (Clontech), respectively. The mutated constructs (V2785A,

Y2793A, K2807A, I2811A, L2791A and I2811A/L2791A) were obtained by site directed mutagenesis.

The lentiCRISPR v2 was a gift from Dr. F. Zhang (Addgene plasmid # 52961). The CRISPR/Cas9 guides were designed using the online tool available at http://zlab.bio/guide-design-resources. The desired 5′ overhangs were added and oligos were phosphorylated, annealed and ligated into the lentiCRISPRv2 predigested with BsmBI.

RNA extraction, RT-PCR and qPCR—Total RNA was purified using Trizol reagent (Ambion, 15596018) accordingly to manufacturer's instructions. 1 mg of RNA was reverse transcribed in cDNA using random hexamers and M-MuLV reverse transcriptase (NEB). qPCRs were assembled with Absolute QPCR ROX Mix (Thermo Scientific, AB-1139), gene-specific oligonucleotides and double-dye probes (see Key Resources Table) and analyzed using the StepOne Plus Real Time PCR system (Applied Biosystem). Data were normalized to the housekeeping gene *glucuronidase β* (*GusB*).

Chromatin ImmunoPrecipitation (ChIP)—ChIP experiments were performed as previously described (Oswald et al., 2016). The following antibodies were used: anti-H3K9ac (abcam, ab4441), anti-H3K27ac (Diagenode, pAb-174–050), anti-H3 (abcam, ab1791), anti-RNAPII (Santa Cruz, sc-899) or IgG (Diagenode, C15410206) as mock control. Experiments were analyzed by qPCR on a StepOnePlus Real-Time PCR System (Applied Biosystem), making use of Absolute QPCR ROX Mix (Thermo Scientific AB-1139), gene-specific oligonucleotides and double-dye probes (see Key Resources Table). Gene desert was used as negative control as previously described (Oswald et al., 2016).

Preparation of protein extracts and Western Blotting from MT cells—Whole Cell Extract (WCE) was prepared as follows. Briefly, cells were washed twice in PBS, lysed in WCE buffer (20 mM Tris-HCl pH 8.0, 150 mM NaCl, 1% NP-40, 10% glycerol, 0.5 mM Na_3VO_4, 10 mM NaF, 1 mM PMSF, 1 x Protease inhibitor cocktail mix) and incubated 20 min on ice. After centrifuging 15 min at 13200 rpm at 4°C, the supernatant was recovered.

The Nuclear Extract (NE) from MT cells overexpressing the SHARP constructs was prepared as follows. Briefly, cells were washed with PBS and resuspended in Buffer A (20 mM HEPES pH 7.9 / 20 mM NaCl / 5 mM $MgCl_2$ / 10% glycerol / 0.2 mM PMSF) at the concentration of 1×10^6 cells/ml. The cell suspension was incubated 20 min on ice and mixed by vortexing. After 5 min centrifugation at 4000 rpm at 4°C, the pellet was washed twice in PBS and resuspended in Buffer C (20 mM HEPES pH 7.9 / 300 mM NaCl / 0.2% NP-40 / 25% glycerol / 1 mM $MgCl_2$/0.2 mM PMSF / 1 x Protease inhibitor mix / 0.3 mM DTT) at the concentration of 1×10^6 nuclei/100 µl. After 20 min of incubation on ice, the nuclei suspension was centrifuged 5 min at 13200 rpm at 4°C and the supernatant was collected.

The NE from MT cells overexpressing the RBPJ constructs was prepared as follows. Briefly, 10×10^6 cells were washed with PBS and resuspended in 200 µL of Buffer 1 (10 mM HEPES pH 7.9 / 10 mM KCl / 0.1 mM EDTA / 0.1 mM EGTA / 1 mM ßME, supplemented

with PMSF). The cell suspension was incubated 10 min on ice, 5 μL of 10% NP-40 were added and mixed by vortexing. After 10 s of centrifugation at 13000 rpm at 4°C, the nuclei pellet was washed twice in 500 mL of Buffer 1 and resuspended in 100 μL of Buffer 2 (20 mM HEPES pH 7.9 / 400 mM NaCl / 1 mM EDTA / 1 mM EGTA / 1 mM ßME, supplemented with PMSF). After 20 min of incubation on ice, the nuclei suspension was centrifuged 10 min at 13000 rpm at 4°C and the supernatant was collected for further analysis.

Protein concentration was measured by Bradford assay (Biorad) and samples were boiled after adding SDS-polyacrylamide gel loading buffer. Samples were resolved by SDS-Page and analyzed by western blotting using antibodies against GAPDH (abcam, ab8245), GFP (Roche, 11814460001) or TBP (Santa Cruz, sc-273). Briefly, membranes were blocked in 5% milk, 1x TBS, 0.1% Tween-20 (TBS-T) and primary antibodies were diluted in 5% milk, TBS-T. After incubation over night at 4°C, membranes were washed in TBS-T, secondary antibodies against mouse (Cell Signaling, #7076S) or rabbit (Cell Signaling, #7074S) were diluted in 5% milk TBS-T and finally membranes were washed in TBS-T.

In the case of the RBPJ western blotting the procedure was as follows. Briefly, membranes were blocked in 5% milk, 1x TBS and the RBPJ antibody (Cosmo Bio Co. LTD, 2ZRBP2) was diluted 1:1000 in 5% BSA, 1x TBS, 0.3% NP40. After incubation over night at 4°C, membranes were washed three times 15 min each in 1x TBS / 0.5 M NaCl / 0.5% Triton X-100 and the secondary antibody against rat (Jackson ImmunoResearch, 112-035-072) was diluted 1:5000 in 5% BSA, 1x TBS, 0.3% NP-40. Membranes were washed three times 15 min each in 1x TBS / 0.5 M NaCl / 0.5% Triton X-100. All membranes were finally incubated with ECL solution and chemiluminescence was detected with a light sensitive film.

QUANTIFICATION AND STATISTICAL ANALYSIS

Quantification of ITC data—ITC binding data are presented as means ± SD from at least three independent experiments.

Number of experiments, statistical test and p values are given in the respective figure legends.

DATA AND SOFTWARE AVAILABILITY

The coordinates and structure factors for the RBPJ-SHARP-DNA X-ray structure have been deposited in the PDB under ID code PDB: 6DKS.

Supplementary Material

Refer to Web version on PubMed Central for supplementary material.

ACKNOWLEDGMENTS

We thank Roswitha Rittelmann, Sabine Schirmer, and Thomas Schmidt-Wöll for excellent technical assistance. This work was supported by NIH grant 5R01CA178974 (to R.A.K.). It was also supported by collaborative research grant TRR81 and grant BO 1639/9–1 by the DFG (German Research Foundation) and the Excellence Cluster for

Cardio Pulmonary System (ECCPS) in Giessen (to T.B.). B.D.G. is supported by a research grant of the University Medical Center Giessen and Marburg (UKGM). This work was further supported by DFG grant SFB1074/A3 and by the BMBF (Federal Ministry of Education and Research, Research Nucleus SySt AR) (to F.O.). L.P. is supported by the DFG (GRK 2253 – HEIST). This research used resources of the Advanced Photon Source, a Department of Energy (DOE) Office of Science User Facility operated for the DOE Office of Science by Argonne National Laboratory under contract DE-AC02–06CH11357.

REFERENCES

Adams PD, Afonine PV, Bunkóczi G, Chen VB, Davis IW, Echols N, Headd JJ, Hung LW, Kapral GJ, Grosse-Kunstleve RW, et al. (2010). PHENIX: a comprehensive Python-based system for macromolecular structure solution. Acta Crystallogr. D Biol. Crystallogr 66, 213–221. [PubMed: 20124702]

Ariyoshi M, and Schwabe JW (2003). A conserved structural motif reveals the essential transcriptional repression function of Spen proteins and their role in developmental signaling. Genes Dev. 17, 1909–1920. [PubMed: 12897056]

Borggrefe T, and Oswald F (2009). The Notch signaling pathway: transcriptional regulation at Notch target genes. Cell. Mol. Life Sci 66, 1631–1646. [PubMed: 19165418]

Braune EB, and Lendahl U (2016). Notch – a goldilocks signaling pathway in disease and cancer therapy. Discov. Med 21, 189–196. [PubMed: 27115169]

Bray SJ (2016). Notch signalling in context. Nat. Rev. Mol. Cell Biol 17, 722–735. [PubMed: 27507209]

Castel D, Mourikis P, Bartels SJ, Brinkman AB, Tajbakhsh S, and Stun-nenberg HG (2013). Dynamic binding of RBPJ is determined by Notch signaling status. Genes Dev. 27, 1059–1071. [PubMed: 23651858]

Chan SKK, Cerda-Moya G, Stojnic R, Millen K, Fischer B, Fexova S, Skalska L, Gomez-Lamarca M, Pillidge Z, Russell S, and Bray SJ (2017). Role of co-repressor genomic landscapes in shaping the Notch response. PLoS Genet. 13, e1007096. [PubMed: 29155828]

Collins KJ, Yuan Z, and Kovall RA (2014). Structure and function of the CSL-KyoT2 corepressor complex: a negative regulator of Notch signaling. Structure 22, 70–81. [PubMed: 24290140]

Davis IW, Leaver-Fay A, Chen VB, Block JN, Kapral GJ, Wang X, Murray LW, Arendall WB, 3rd, Snoeyink J, Richardson JS, and Richardson DC (2007). MolProbity: all-atom contacts and structure validation for proteins and nucleic acids. Nucleic Acids Res. 35, W375–W383. [PubMed: 17452350]

Del Bianco C, Aster JC, and Blacklow SC (2008). Mutational and energetic studies of Notch 1 transcription complexes. J. Mol. Biol 376, 131–140. [PubMed: 18155729]

Emsley P, and Cowtan K (2004). Coot: model-building tools for molecular graphics. Acta Crystallogr. D Biol. Crystallogr 60, 2126–2132. [PubMed: 15572765]

Friedmann DR, Wilson JJ, and Kovall RA (2008). RAM-induced allostery facilitates assembly of a notch pathway active transcription complex. J. Biol. Chem 283, 14781–14791. [PubMed: 18381292]

Giaimo BD, Ferrante F, and Borggrefe T (2017). Chromatin Immunoprecipitation (ChIP) in Mouse T-cell Lines. J. Vis. Exp, Published online June 17, 2017. 10.3791/55907.

Giaimo BD, Ferrante F, Vallejo DM, Hein K, Gutierrez-Perez I, Nist A, Stiewe T, Mittler G, Herold S, Zimmermann T, et al. (2018). Histone variant H2A.Z deposition and acetylation directs the canonical Notch signaling response. Nucleic Acids Res. 46, 8197–8215. [PubMed: 29986055]

Johnson SE, Ilagan MX, Kopan R, and Barrick D (2010). Thermodynamic analysis of the CSL x Notch interaction: distribution of binding energy of the Notch RAM region to the CSL beta-trefoil domain and the mode of competition with the viral transactivator EBNA2. J. Biol. Chem 285, 6681–6692. [PubMed: 20028974]

Kovall RA, and Blacklow SC (2010). Mechanistic insights into Notch receptor signaling from structural and biochemical studies. Curr. Top. Dev. Biol 92, 31–71. [PubMed: 20816392]

Kovall RA, and Hendrickson WA (2004). Crystal structure of the nuclear effector of Notch signaling, CSL, bound to DNA. EMBO J. 23, 3441–3451. [PubMed: 15297877]

Kovall RA, Gebelein B, Sprinzak D, and Kopan R (2017). The Canonical Notch Signaling Pathway: Structural and Biochemical Insights into Shape, Sugar, and Force. Dev. Cell 41, 228–241. [PubMed: 28486129]

Krissinel E, and Henrick K (2007). Inference of macromolecular assemblies from crystalline state. J. Mol. Biol 372, 774–797. [PubMed: 17681537]

Kuroda K, Han H, Tani S, Tanigaki K, Tun T, Furukawa T, Taniguchi Y, Kurooka H, Hamada Y, Toyokuni S, and Honjo T (2003). Regulation of marginal zone B cell development by MINT, a suppressor of Notch/RBP-J signaling pathway. Immunity 18, 301–312. [PubMed: 12594956]

Lubman OY, Ilagan MX, Kopan R, and Barrick D (2007). Quantitative dissection of the Notch:CSL interaction: insights into the Notch-mediated transcriptional switch. J. Mol. Biol 365, 577–589. [PubMed: 17070841]

Maier D (2006). Hairless: the ignored antagonist of the Notch signalling pathway. Hereditas 143, 212–221. [PubMed: 17362357]

Maier D, Kurth P, Schulz A, Russell A, Yuan Z, Gruber K, Kovall RA, and Preiss A (2011). Structural and functional analysis of the repressor complex in the Notch signaling pathway of Drosophila melanogaster. Mol. Biol. Cell 22, 3242–3252. [PubMed: 21737682]

McCoy AJ, Grosse-Kunstleve RW, Adams PD, Winn MD, Storoni LC, and Read RJ (2007). Phaser crystallographic software. J. Appl. Cryst 40, 658–674. [PubMed: 19461840]

Moon AF, Mueller GA, Zhong X, and Pedersen LC (2010). A synergistic approach to protein crystallization: combination of a fixed-arm carrier with surface entropy reduction. Protein Sci 19, 901–913. [PubMed: 20196072]

Nam Y, Sliz P, Song L, Aster JC, and Blacklow SC (2006). Structural basis for cooperativity in recruitment of MAML coactivators to Notch transcription complexes. Cell 124, 973–983. [PubMed: 16530044]

Newberry EP, Latifi T, and Towler DA (1999). The RRM domain of MINT, a novel Msx2 binding protein, recognizes and regulates the rat osteocalcin promoter. Biochemistry 38, 10678–10690. [PubMed: 10451362]

Ntziachristos P, Lim JS, Sage J, and Aifantis I (2014). From fly wings to targeted cancer therapies: a centennial for notch signaling. Cancer Cell 25, 318–334. [PubMed: 24651013]

Oswald F, Kostezka U, Astrahantseff K, Bourteele S, Dillinger K, Zechner U, Ludwig L, Wilda M, Hameister H, Knöchel W, et al. (2002). SHARP is a novel component of the Notch/RBP-Jkappa signalling pathway. EMBO J. 21, 5417–5426. [PubMed: 12374742]

Oswald F, Rodriguez P, Giaimo BD, Antonello ZA, Mira L, Mittler G, Thiel VN, Collins KJ, Tabaja N, Cizelsky W, et al. (2016). A phosphodependent mechanism involving NCoR and KMT2D controls a permissive chromatin state at Notch target genes. Nucleic Acids Res. 44, 4703–4720. [PubMed: 26912830]

Shi Y, Downes M, Xie W, Kao HY, Ordentlich P, Tsai CC, Hon M, and Evans RM (2001). Sharp, an inducible cofactor that integrates nuclear receptor repression and activation. Genes Dev. 15, 1140–1151. [PubMed: 11331609]

Siebel C, and Lendahl U (2017). Notch Signaling in Development, Tissue Homeostasis, and Disease. Physiol. Rev 97, 1235–1294. [PubMed: 28794168]

Smart OS, Womack TO, Flensburg C, Keller P, Paciorek W, Sharff A, Vonrhein C, and Bricogne G (2012). Exploiting structure similarity in refine ment: automated NCS and target-structure restraints in BUSTER. Acta Crystallogr. D Biol. Crystallogr 68, 368–380. [PubMed: 22505257]

Surendran K, Boyle S, Barak H, Kim M, Stomberski C, McCright B, and Kopan R (2010). The contribution of Notch1 to nephron segmentation in the developing kidney is revealed in a sensitized Notch2 background and can be augmented by reducing Mint dosage. Dev. Biol 337, 386–395. [PubMed: 19914235]

Tabaja N, Yuan Z, Oswald F, and Kovall RA (2017). Structure-function analysis of RBP-J-interacting and tubulin-associated (RITA) reveals regions critical for repression of Notch target genes. J. Biol. Chem 292, 10549–10563. [PubMed: 28487372]

Taniguchi Y, Furukawa T, Tun T, Han H, and Honjo T (1998). LIM protein KyoT2 negatively regulates transcription by association with the RBP-J DNA-binding protein. Mol. Cell. Biol 18, 644–654. [PubMed: 9418910]

Tsuji M, Shinkura R, Kuroda K, Yabe D, and Honjo T (2007). Msx2-interacting nuclear target protein (Mint) deficiency reveals negative regulation of early thymocyte differentiation by Notch/RBP-J signaling. Proc. Natl. Acad. Sci. USA 104, 1610–1615. [PubMed: 17242367]

VanderWielen BD, Yuan Z, Friedmann DR, and Kovall RA (2011). Transcriptional repression in the Notch pathway: thermodynamic characterization of CSL-MINT (Msx2-interacting nuclear target protein) complexes. J. Biol. Chem 286, 14892–14902. [PubMed: 21372128]

Wacker SA, Alvarado C, von Wichert G, Knippschild U, Wiedenmann J, Clauss K, Nienhaus GU, Hameister H, Baumann B, Borggrefe T, et al. (2011). RITA, a novel modulator of Notch signalling, acts via nuclear export of RBP-J. EMBO J. 30, 43–56. [PubMed: 21102556]

Wilson JJ, and Kovall RA (2006). Crystal structure of the CSL-Notch-Mastermind ternary complex bound to DNA. Cell 124, 985–996. [PubMed: 16530045]

Xu T, Park SS, Giaimo BD, Hall D, Ferrante F, Ho DM, Hori K, Anhezini L, Ertl I, Bartkuhn M, et al. (2017). RBPJ/CBF1 interacts with L3MBTL3/MBT1 to promote repression of Notch signaling via histone demethylase KDM1A/LSD1. EMBO J. 36, 3232–3249. [PubMed: 29030483]

Yuan Z, Friedmann DR, VanderWielen BD, Collins KJ, and Kovall RA (2012). Characterization of CSL (CBF-1, Su(H), Lag-1) mutants reveals differences in signaling mediated by Notch1 and Notch2. J. Biol. Chem 287, 34904–34916. [PubMed: 22915591]

Yuan Z, Praxenthaler H, Tabaja N, Torella R, Preiss A, Maier D, and Kovall RA (2016). Structure and Function of the Su(H)-Hairless Repressor Complex, the Major Antagonist of Notch Signaling in Drosophila melanogaster. PLoS Biol. 14, e1002509. [PubMed: 27404588]

Zehender A, Bayer M, Bauer M, Zeis B, Preiss A, and Maier D (2017). Conservation of the Notch antagonist Hairless in arthropods: functional analysis of the crustacean Daphnia pulex Hairless gene. Dev. Genes Evol 227, 339–353. [PubMed: 28861687]

Highlights

- The corepressor SHARP binds the transcription factor RBPJ in a bipartite manner
- SHARP binds the BTD and CTD of RBPJ, using motifs analogous to other corepressors
- Structure-based mutants affect RBPJ-SHARP complex formation *in vitro* and in cells
- RBPJ mutants are defective in repression from Notch target genes in cells

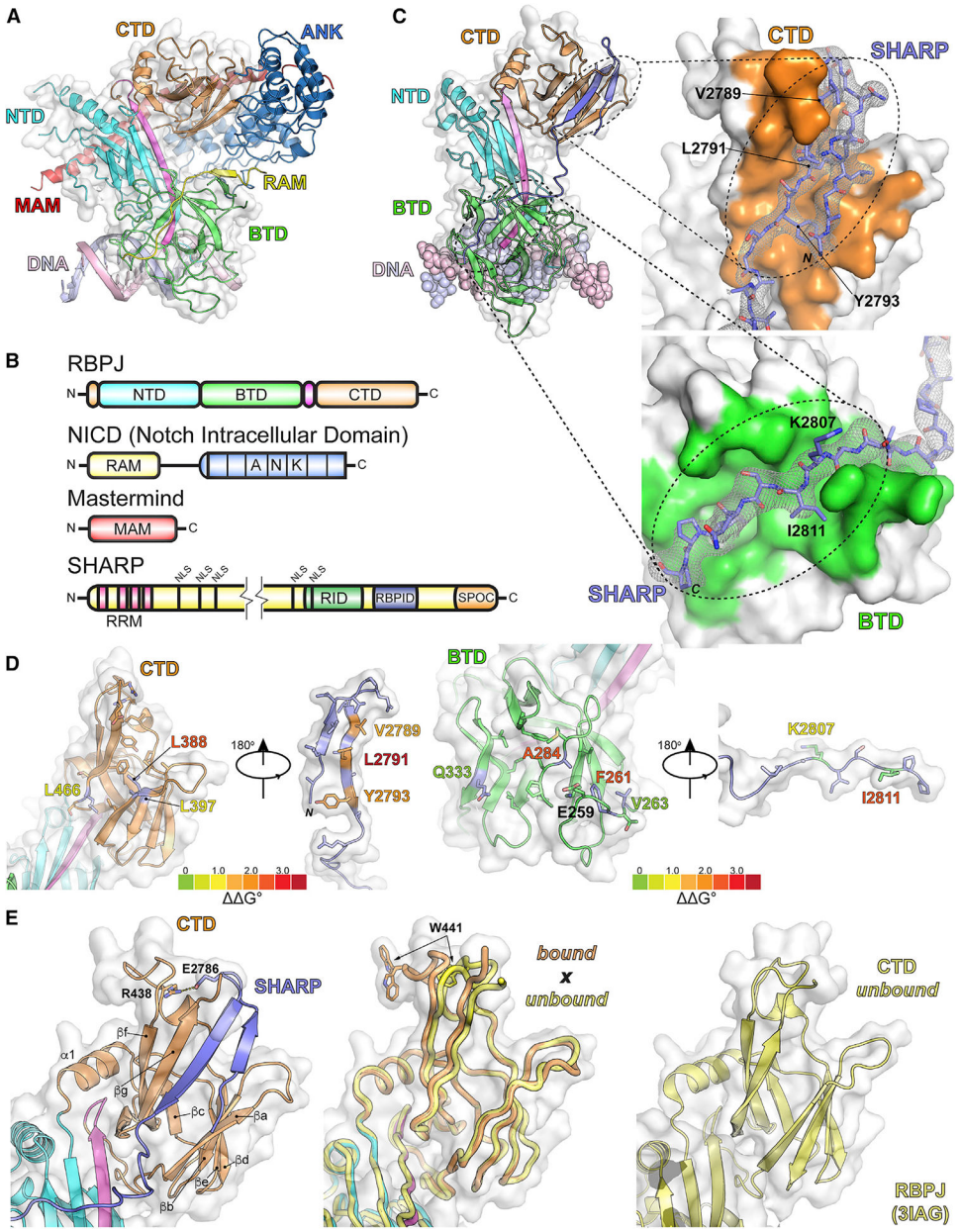

Figure 1. X-Ray Structure of the RBPJ-SHARP Corepressor Complex Bound to DNA

(A) Structure of the *C. elegans* RBPJ-NICD-MAM ternary complex bound to DNA (PDB: 2FO1). RBPJ is composed of three domains: the NTD (N-terminal domain), BTD (β-trefoil domain), and CTD (C-terminal domain), which are colored cyan, green, and orange, respectively. A β strand that makes hydrogen-bonding interactions with all three domains is colored magenta. The RAM and ANK domains of NICD are colored yellow and blue, respectively. MAM and DNA are colored red and light pink-blue, respectively.

(B) Domain schematics of RBPJ, NICD, and MAM, colored similarly to the structure. SHARP is a multidomain transcriptional coregulator that contains N-terminal RRM (RNA recognition motif) domains, multiple NLSs (nuclear localization sequences), an RID

(receptor interaction domain), an RBPID (RBPJ-interacting domain), and a C-terminal SPOC (Spen paralog and ortholog C-terminal) domain.

(C) Ribbon diagram of the RBPJ-SHARP-DNA complex, with RBPJ and the DNA colored, as in (A), and SHARP is colored purple. Also shown are magnified views of the interaction of SHARP with the CTD (top) and BTD (bottom) of RBPJ. RBPJ is represented as a molecular surface, with CTD and BTD residues that contact SHARP colored orange and green, respectively. SHARP is shown in a stick representation, with carbon, oxygen, and nitrogen atoms colored purple, red, and blue, respectively. Electron density (composite omit map contoured at 1σ) corresponding to SHARP is colored gray. SHARP residues that were mutated and tested for activity are labeled. See also Figure S5.

(D) Open book representation of RBPJ-SHARP interfaces. Left: CTD-SHARP interface. Right: BTD-SHARP interface. Side chains that contribute to the interface are shown. Key residues at the interface that were mutated and tested for activity are labeled and color-coded according to ΔΔG°. See also Figure S1.

(E) Conformational changes in the CTD of RBPJ as a result of SHARP binding. Left: the CTD-SHARP complex with labeled secondary structural elements of the CTD. The R438-E2786 salt bridge is also shown. Center: structural overlay of RBPJ (bound) from the RBPJ-SHARP complex with an unbound structure of RBPJ (PDB: 3IAG). The RBPJ bound and unbound structures are colored orange and yellow, respectively. RBPJ residue W441, which undergoes a large conformational change in the bound structure, is shown. Right: ribbon diagram of the unbound RBPJ structure (PDB: 3IAG).

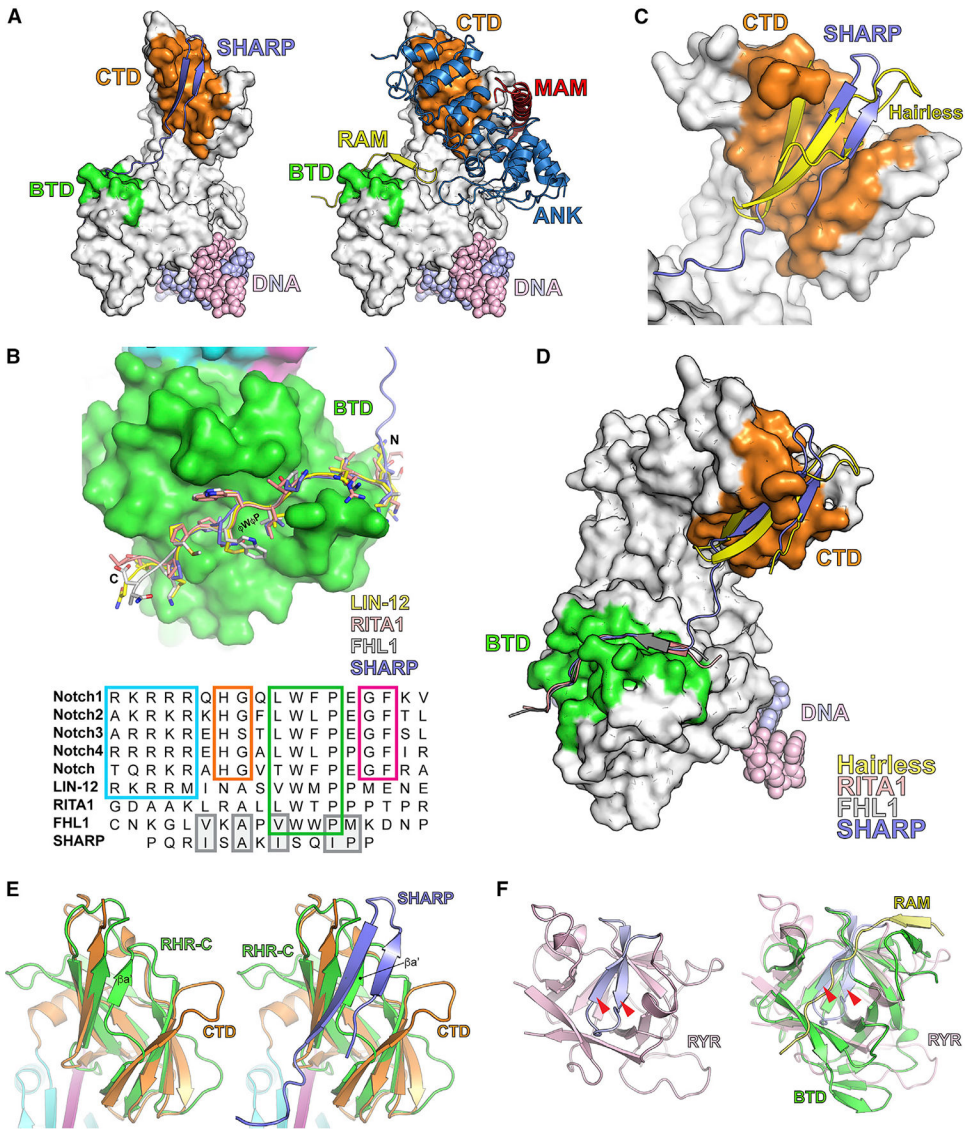

Figure 2. Comparison of Coregulator Binding Sites on RBPJ

(A) Both SHARP and NICD bind the BTD and CTD of RBPJ. Left: RBPJ-SHARP-DNA complex structure, with RBPJ represented as a gray molecular surface, SHARP as a ribbon diagram colored purple, and the DNA as CPK colored light blue and pink. The RBPJ residues that contact SHARP in the BTD and CTD are colored green and orange, respectively. Right: *C. elegans* RBPJ-NICD-MAM-DNA complex structure (PDB: 2FO1), with RBPJ represented as a gray molecular surface. NICD is represented as a ribbon diagram, with its RAM and ANK domains colored yellow and blue, respectively. MAM is depicted as a ribbon diagram and colored red. The DNA is colored light blue and pink.

(B) Structural alignment of SHARP and other coregulators that bind the BTD of RBPJ. Top: the BTD of RBPJ is represented as a green molecular surface. SHARP, the RAM domain from LIN-12, RITA1, and FHL1 are colored purple, yellow, light pink, and gray, respectively. The hydrophobic tetrapeptide (ϕWϕP) is labeled. Bottom: sequence alignment of coregulators that bind the BTD of RBPJ, including the RAM domains of Notch from

mammals, *D. melanogaster*, and *C. elegans*, and the corepressors RITA1, FHL1, and SHARP. The conserved ϕWϕP is boxed in green. Other conserved regions in RAM that contribute to binding are highlighted, including the basic region (blue), the -HG- motif (orange), and the -GF- motif (magenta). Structurally similar residues in SHARP that align with other BTD binders are boxed and highlighted in gray.

(C) Structural similarity of RBPJ-SHARP and Su(H)-Hairless corepressor complexes. Su(H) is represented as a gray molecular surface, with the SHARP and Hairless binding sites colored orange. SHARP and Hairless are shown as ribbon diagrams and colored purple and yellow, respectively.

(D) Overview of corepressor binding to RBPJ, illustrating the bipartite binding of SHARP. RBPJ is represented as a gray molecular surface, with its BTD and CTD binding clefts colored green and orange, respectively. The corepressors SHARP, Hairless, RITA1, and FHL1 are shown as ribbon diagrams and colored purple, yellow, pink, and gray, respectively. The DNA is colored light blue and light pink.

(E) Structural comparison of the CTD of RBPJ with the RHR-C domain of NFAT. RBPJ-SHARP is colored as in Figure 1, and NFAT is colored green. The NFAT β strand βa', which is absent in the CTD of RBPJ but occupied by SHARP in the complex structure, is labeled.

(F) Structural alignment of the BTD from RBPJ with a canonical β-trefoil fold from the ryanodine receptor (RYR). A canonical BTD is composed of 12 β strands, in which four β strands are arranged in a pseudo-threefold symmetrical arrangement. The atypical BTD of RBPJ is missing two of the 12 β strands that compose a canonical BTD. The BTDs of RBPJ and RYR are colored green and light pink, respectively. The two β strands that are missing in the RBPJ BTD fold are colored light blue and highlighted with red arrowheads. The RAM domain of NICD is colored yellow.

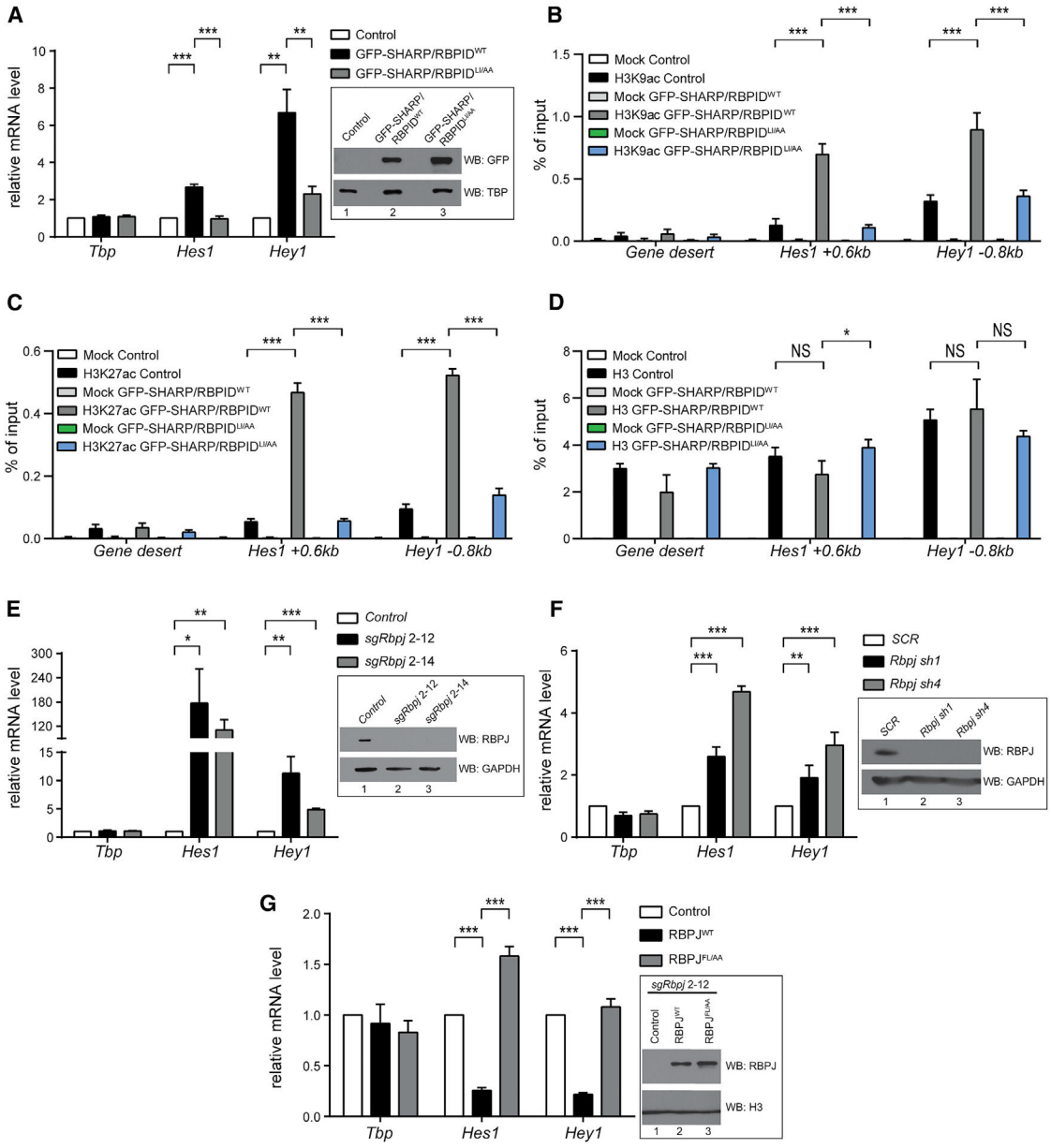

Figure 3. The RBPJ-SHARP Interaction Is Required for Repression of Notch Target Genes in Cells

(A) The wild-type SHARP RBPID (RBPID^{WT}), but not the RBPJ-interacting defective SHARP RBPID (RBPID$^{LI/AA}$) mutant, causes upregulation of Notch target genes in mouse mature T (MT) cells by outcompeting endogenous SHARP for RBPJ binding. MT cells were infected with plasmids encoding GFP-tagged SHARP (2,776–2,833), either wild-type (GFP-SHARP/RBPID^{WT}, black bars) or the RBPJ-interacting defective mutant L2791A/I2811A (GFP-SHARP/RBPID$^{LI/AA}$, gray bars) or an empty vector control (Control, white bars). Left: total RNA from MT cells was analyzed by qPCR using primers specific for *Tbp*, *Hes1*, or *Hey1*. Data shown represent the mean ± SD of triplicate experiments (**p < 0.01, ***p < 0.001, unpaired Student's t test). Right: nuclear extracts (NEs) were prepared from MT cells and analyzed by western blotting, with TBP used as a loading control.

(B–D) GFP-SHARP/RBPID^{WT} derepresses Notch target genes via histone deacetylation. MT cells were infected with plasmids encoding GFP-SHARP/RBPID^{WT}, GFP-SHARP/RBPID$^{LI/AA}$, or an empty vector control and analyzed by chromatin immunoprecipitation (ChIP) using antibodies against H3K9ac (B), H3K27ac (C), or H3 (D). The enrichment was analyzed by qPCR on the enhancers of *Hes1* and *Hey1*, located at approximately +0.6 kb and −0.8 kb relative to the transcription start site, respectively. *Gene desert* was used as a negative control. Data were normalized to the positive control (*Gapdh 0kb*), and, in the case of the H3K9ac and H3K27ac ChIP, data were further normalized to histone occupancy (H3). Shown is the mean ± SD of two experiments measured twice each (NS, not significant; *p < 0.05; ***p < 0.001; unpaired Student's t test). See also Figure S4.

(E) RBPJ is required to repress the Notch target genes *Hes1* and *Hey1* in MT cells, as revealed by CRISPR/Cas9 depletion of RBPJ. Left: total RNA from wild-type (control) or RBPJ-depleted (clones *sgRbpj 2–12* and *sgRbpj 2–14*) MT cells was analyzed by qPCR. Shown is the mean ± SD of triplicate experiments (*p < 0.05, **p < 0.01, ***p < 0.001, unpaired Student's t test). Right: whole-cell extracts (WCEs) were prepared from MT cells and analyzed by western blotting using an anti-RBPJ antibody. GAPDH was used as loading control.

(F) *Hes1* and *Hey1* Notch target genes are upregulated upon shRNA-mediated *Rbpj* knockdown but not with the *SCR* control shRNA. Left: total RNA from MT cells infected with shRNAs targeting *Rbpj* (*Rbpj sh1* or *Rbpj sh4*) or scrambled shRNA control (SCR) was analyzed by qPCR using primers specific for *Tbp*, *Hes1*, or *Hey1*. Shown is the mean ± SD of quadruplicate experiments (**p < 0.01, ***p < 0.001, unpaired Student's t test). Right: WCE was prepared from MT cells and analyzed by western blotting using an RBPJ antibody. GAPDH was used as a loading control.

(G) Expression of RBPJ^{WT} but not RBPJ$^{FL/AA}$ in the RBPJ-depleted background rescues the repression of Notch target genes. Left: total RNA from *sgRbpj 2–12* MT cells infected with empty vector (control), RBPJ^{WT}, or RBPJ$^{FL/AA}$ was analyzed by qPCR using primers specific for *Tbp*, *Hes1*, or *Hey1*. Shown is the mean± SD of three independent experiments measured twice each (*p < 0.05, **p < 0.01, ***p < 0.001, unpaired Student's t test). Right: NEs were prepared from *sgRbpj 2–12* MT cells infected with empty vector (control), RBPJ^{WT}, or RBPJ$^{FL/AA}$ and analyzed by western blotting using anti-RBPJ antibodies. Histone H3 was used as a loading control.

Table 1.

RBPJ-SHARP Calorimetric Binding Data for Native and Mutant Proteins

RBPJ	SHARP	K (M^{-1})	K_d (μM)	ΔG° (kcal/mol)	ΔH° (kcal/mol)	−TΔS° (kcal/mol)	ΔΔG° (kcal/mol)
WT	WT	$2.0 \pm 0.5 \times 10^8$	0.005	−11.3 ± 0.1	−13.5 ± 0.4	2.2 ± 0.3	NA
WT	V2789A	$1.9 \pm 1.3 \times 10^7$	0.067	−9.9 ± 0.4	−11.0 ± 0.9	1.1 ± 1.2	1.4
WT	L2791A	$5.8 \pm 1.0 \times 10^5$	1.75	−7.9 ± 0.1	−7.8 ± 0.8	−0.1 ± 0.7	3.4
WT	Y2793A	$8.7 \pm 2.5 \times 10^6$	0.122	−9.4 ± 0.2	−9.0 ± 0.2	−0.4 ± 0.4	1.9
WT	K2807A	$3.6 \pm 0.8 \times 10^7$	0.029	−10.3 ± 0.2	−13.3 ± 0.1	3.0 ± 0.1	1.0
WT	I2811A	$3.3 \pm 0.6 \times 10^6$	0.316	−8.9 ± 0.1	−12.3 ± 0.2	3.4 ± 0.2	2.4
WT	L2791A/I2811A	NBD	NA	NA	NA	NA	NA
F261A	WT	$4.5 \pm 0.9 \times 10^6$	0.23	−9.1 ± 0.1	−9.9 ± 0.5	0.8 ± 0.4	2.2
V263A	WT	$3.2 \pm 0.4 \times 10^8$	0.003	−11.6 ± 0.1	−18.3 ± 0.8	6.7 ± 0.9	−0.3
A284V	WT	$4.0 \pm 1.0 \times 10^6$	0.27	−9.0 ± 0.2	−12.9 ± 0.6	3.9 ± 0.7	2.3
Q333A	WT	$2.6 \pm 0.3 \times 10^8$	0.004	−11.4 ± 0.1	−16.8 ± 0.7	5.4 ± 0.7	−0.1
L386A	WT	$7.5 \pm 3.5 \times 10^7$	0.016	−10.7 ± 0.3	−13.2 ± 0.4	2.5 ± 0.7	0.6
L388A	WT	$2.6 \pm 0.5 \times 10^6$	0.391	−8.7 ± 0.1	−7.5 ± 0.6	−1.2 ± 0.7	2.6
L397A	WT	$4.2 \pm 0.8 \times 10^7$	0.025	−10.4 ± 0.1	−11.3 ± 0.2	0.9 ± 0.3	0.9
L466A	WT	$9.6 \pm 2.4 \times 10^7$	0.011	−10.9 ± 0.1	−13.3 ± 0.2	2.4 ± 0.2	0.4
F261A/L388A	WT	NBD	NA	NA	NA	NA	NA

All experiments were performed at 25°C. NBD, no binding detected. See also Figure S1.

KEY RESOURCES TABLE

REAGENT or RESOURCE	SOURCE	IDENTIFIER
Antibodies		
anti-Flag-M2-agarose	Merck	A2220
anti-GFP	Merck	11814460001
anti-mouse-POD	GE healthcare	NA931V
anti-Flag-M5	Merck	F4042
H3K9ac	abcam	ab4441
H3K27ac	Diagenode	pAb-174-050
H3	abcam	ab1791
RNAPII	Santa Cruz	sc-899
IgG	Diagenode	C15410206
GAPDH	abcam	ab8245
GFP	Roche	11814460001
TBP	Santa Cruz	sc-273
RBPJ	Cosmo Bio Co. LTD	2ZRBP2
Bacterial and Virus Strains		
E. coli STBL3	Thermo Fisher	C7373-03
Chemicals, Peptides, and Recombinant Proteins		
RBPJ aa53-474 and mutants	(Friedmann et al., 2008)	N/A
mbp-SHARP aa2776-2833	This paper	N/A
SMT3-SHARP aa2776-2833 and mutants	This paper and (VanderWielen et al., 2011)	N/A
CHAPS	Roth	1479.2
DTT	Merck	D9163
Bradford-Assay	Biorad	500-0006
Sybrgreen PCR Mastermix	Thermo Fisher	4312704
poly(dI-dC)	GE healthcare	27-7880-03
X-ray films	GE healthcare	28906837
Paraformaldehyde	Merck	1.04005.1000
PMSF	Merck	P7626
cOmplete Mix	Merck	11697498001
PVDV Immobilon-P membrane	Merck	IPVH00010
(Z)-4-hydroxytamoxifen (4-OHT)	Sigma-Aldrich	H7904-5MG
puromycin	Serva	33835
Critical Commercial Assays		
Lipofectamine 2000	Thermo Fisher	11668-019
Profectin© Mammalian Transfection System	Promega	E1200
TNT-Assay (T7)	Promega	L4610
ProLong Gold antifade reagent with DAPI	Thermo Fisher	P36931
Luciferase Assay System	Promega	E1501
QuikChange II XL Site-Directed Mutagenesis Kit	Agilent	200521-5

REAGENT or RESOURCE	SOURCE	IDENTIFIER
Deposited Data		
RBPJ/MBP-SHARP/DNA X-ray structure	This paper	PDB: 6DKS
Experimental Models: Cell Lines		
HeLa	ATCC	CCL2
HEK293	ATCC	CRL1573
Phoenix™	Orbigen	N/A
Hybridoma mature T cells	(Giaimo et al., 2017)	N/A
Oligonucleotides		
See Table S2	N/A	N/A
Recombinant DNA		
pGEX-6p-1-RBPJ aa53-474 and mutants	This paper and (Friedmann et al., 2008)	N/A
pMAL-SHARP aa2776-2833	This paper	N/A
pSMT-SHARP aa2776-2833 and mutants	This paper and (VanderWielen et al., 2011)	N/A
pMIGR1 pSV40-Puro	this paper and (Giaimo et al., 2018)	N/A
pcDNA3.1.Flag-2-mRBPJ	this paper	N/A
pcDNA3.1.Flag-2-mRBPJDstop	this paper	N/A
pFA-CMV	Stratagene	219036
pcDNA3.1-Flag-2-mRBPJ-VP16	this paper	N/A
pMY-Bio-IRES-Blasticidin	this paper	N/A
pFA-CMV-SHARP-2776-2833(wt)	this paper	N/A
Software and Algorithms		
Pymol	The PyMOL Molecular Graphics System, Version 2.0 Schrödinger, LLC.	https://pymol.org/2/
Phenix	Adams et al., 2010	https://www.phenix-online.org/
Coot	Emsley and Cowtan, 2004	https://www2.mrc-lmb.cam.ac.uk/personal/pemsley/coot/
Buster	Global Phasing Ltd	https://www.globalphasing.com/buster/